

ARTICLE

Open Access

C₆₀/Na₄FeO₃/Li₃V₂(PO₄)₃/soft carbon quaternary hybrid superstructure for high-performance battery-supercapacitor hybrid devices

Xudong Zhang¹, Xiaolong Xu¹, Yuebo Hu¹, Guogang Xu², Wen He¹ and Jiefang Zhu³

Abstract

To develop battery-supercapacitor hybrid devices with high energy and power densities, we propose a rational design of a quaternary hybrid superstructure by using a high-energy biotemplate. This new superstructure is composed of stable fullerene C₆₀ nanocages, electroactive Na₄FeO₃, high-energy Li₃V₂(PO₄)₃ and soft carbon as well as tubular ordered mesoporous channels. This design takes advantage of the unique properties of each component, resulting in nanocomposites with synergistic effects to improve the charge transfer and energy storage. We found that this quaternary hybrid electrode has both high energy and power densities as well as a long cycling life in a Li/Na mixed-ion electrolyte, outperforming a multitude of other battery-supercapacitor hybrid devices reported thus far. The charge storage mechanisms of this hybrid superstructure are proposed for optimizing the electrode design.

Introduction

Hybrid energy-storage devices can break the energy density limitation of traditional electrochemical capacitors and the kinetic limitation of batteries. The attainment of both a high power density and a high energy density in one device is highly challenging yet critically important for many applications^{1–3}. The inherent limitations in cation chemistry make lithium-ion batteries (LIBs) and sodium-ion batteries (SIBs) unable to meet the growing demands for electric vehicles and grid-scale energy storage. Therefore, chemistries beyond the Li ion and Na ion, such as the merging of battery and supercapacitor chemistries, are currently being investigated. In recent years, hybrid energy-storage devices, such as battery-supercapacitor hybrid devices (BSHs) based on a battery electrode and a supercapacitor electrode, have received significant attention^{4–6}. The nanostructured hybrid

electrodes enable the integration of the high energy from batteries with a high power and the long lifetime from supercapacitors. The hybrid electrodes can display different charge storage properties, such as capacitive, pseudocapacitive and battery-like behavior, depending on the charge storage guest ion, electrode design, and electrode material selection, structure, morphology, and particle size⁷. The hybrid electrode combines several electroactive materials (such as pseudocapacitive metal oxides, conductive additives, and conducting polymers) in a single electrode. In addition, the integration of hybrid materials takes advantage of the synergy of different components, significantly improving the electrochemical performance^{8–13}. However, a good understanding of the surface chemical interactions between the components and of synergistic effects to enhance the charge transfer and storage is extremely important and currently lacking for hybrid materials.

The selection of appropriate electrode materials and the design of unique hybrid electrodes are key factors in enhancing the electrochemical performance of BSHs. Various binary and ternary hybrid electrodes, such as V₂O₅ nanowire/CNT hybrids¹⁴, MnO₂/Au (shell/core)

Correspondence: Wen He (hewen1960@126.com) or Jiefang Zhu (jiefang.zhu@kemi.uu.se)

¹Institute of Materials Science and Engineering, Qilu University of Technology (Shandong Academy of Sciences), Jinan 250353, China

²Institute of Materials Science and Engineering, Shandong University of Science and Technology, Qingdao 266590, China

Full list of author information is available at the end of the article.

© The Author(s) 2020



Open Access This article is licensed under a Creative Commons Attribution 4.0 International License, which permits use, sharing, adaptation, distribution and reproduction in any medium or format, as long as you give appropriate credit to the original author(s) and the source, provide a link to the Creative Commons license, and indicate if changes were made. The images or other third party material in this article are included in the article's Creative Commons license, unless indicated otherwise in a credit line to the material. If material is not included in the article's Creative Commons license and your intended use is not permitted by statutory regulation or exceeds the permitted use, you will need to obtain permission directly from the copyright holder. To view a copy of this license, visit <http://creativecommons.org/licenses/by/4.0/>.

nanowires¹⁵, MoO₃/TiO₂¹⁶, V₂O₅/polypyrrole¹⁷, MnO₂/graphene/PEDOT-PSS¹⁸, and MnO₂/graphene/PANI¹⁹, have been investigated. However, these hybrid electrodes working in organic electrolytes showed poor charge–discharge reversibility and low specific energy at high rates. Recently, studies found that hybrid electrodes with higher specific capacities, excellent electronic and ionic conductivity, and pseudocapacitive behavior could break the energy density limitation of traditional electrochemical capacitors and the kinetic limitation of batteries². However, the charge storage mechanisms in hybrid structures have drawn much less attention. In addition, quaternary hybrid superstructures that can undergo reversible mixed-ion intercalation are very rare^{20–23}. Recently, it was shown that metal-organic frameworks (MOFs) with unique porous structures, very large pore volumes, ultrahigh specific surface areas and tunable pore sizes can accommodate large guest molecules^{24–29}. Most importantly, they can not only absorb and interact with large guest molecules on the outer and inner surfaces of their continuously interconnected macroporous structures but also exhibit fascinating nanoconfinement effects in their mesochannels^{30–33}. In addition, the porous framework also tolerates the expansion and strain relaxation during reversible electrochemical energy-storage processes; particularly, ordered mesoporous channels may shorten the transport path of electrons and ions and drastically increase the number of active sites with high accessibility^{34–37}. Therefore, the assembly of hybrid materials into an ordered mesoporous framework is an elaborate strategy for the fabrication of high-performance BSHs.

In solid-state physics, a superstructure is an additional structure superimposed on a given crystalline structure. A typical and important example is the nanoparticle superstructure. The integration and organized assembly of different nanoparticle blocks generate nanoparticle superstructures with different physicochemical properties due to the synergistic effect of different nanoparticles³⁸. These nanoparticle superstructures have received increasing attention as promising electrode materials in energy-storage devices because of their distinct mechanical, electronic, and electrochemical properties that derive from the size, shape, composition, and 3D assembly of their component nanoparticle blocks^{39–43}. Recently, Zhang et al.⁴⁴ designed and fabricated 3D advanced MXene/Si-based superstructures for boosting lithium-ion batteries (LIBs). This superstructure anode delivers a stable capacity of 390 mAh g⁻¹ with 99.9% coulombic efficiency and 76.4% capacity retention after 1000 cycles at 10 C. Zuo et al.⁴⁵ synthesized a high-capacity O₂-type Li-rich cathode material with a single-layer Li₂MnO₃ superstructure. This superstructure cathode for lithium-ion batteries can deliver an extraordinary reversible

capacity of 400 mAh g⁻¹ (energy density of 1360 Wh kg⁻¹). The results show that the superstructures will further the development of high-capacity electrode materials and high energy density batteries.

A fullerene (C₆₀) nanocage is a zero-dimensional material with many novel physical and chemical properties^{46,47}. C₆₀ and inorganic–organic clusters and nanocrystals can assemble into superstructured materials with tailorable properties⁴⁸, which can provide a highly conductive network for ensuring fast ion transport and an elastic buffer for volume changes⁴⁹. Adenosine triphosphate disodium (Na₂ATP) is a biomolecule and has an ordered carbon compound backbone in its structure, and its critical part is triphosphate with high-energy phosphorus bonds. The results of our work have shown that Na₂ATP is also a multifunctional high-energy biotemplate for the synthesis of highly active electrode materials^{50,51}. It was used not only as a carbon source of C₆₀ and a nanostructure template but also as a phosphorus source that provided many reactive sites and phosphorus bonds for the synthesis of high-energy nanoparticles. Herein, we introduce a new design concept in which a quaternary hybrid superstructured electrode is based on the reversible insertion/deinsertion of Li⁺/Na⁺/PF₆⁻/ClO₄⁻ mixed ions. This quaternary hybrid superstructured electrode not only exhibits improvements in both the energy and power density performances but also takes advantage of the synergistic effect of the ordered mesoporous superstructure and different nanoparticles. The C₆₀/Na₄FeO₃ (NFO)/high-energy Li₃V₂(PO₄)₃ (HE-LVP)/soft carbon (SC) hybrid electrode was prepared using (Na₂ATP) as sodium, phosphorus and carbon sources via freeze drying and heat treatment. Notably, this C₆₀/NFO/HE-LVP/SC quaternary hybrid electrode maintains an ultrahigh energy density of 405 Wh kg⁻¹ (power density of 413 W kg⁻¹) after 300 cycles at 10 C, which is thus far the highest value among the reported Li-ion and Na-ion BSHs (see Supplementary Table S1). These improvements mostly originate from the combinations of different energy-storage mechanisms in the superstructure.

Several merits of this design are as follows: (1) the C₆₀ nanocages not only possess high conductivity, good Li⁺/Na⁺ storage property and mechanical stability but also show an extra intercalation pseudocapacitance; (2) NFO is a good electroactive electrode that provides an extra redox pseudocapacitance; (3) the high-energy LVP nanoparticles contribute to the excellent battery-type electrochemistry via reversible redox reactions, resulting in high energy density and cyclability; and (4) the tubular ordered mesoporous channels provide PF₆⁻/ClO₄⁻ anion intercalation via adsorption and electrostatic accumulation of charges on the electrode–electrolyte

interface, contributing to a high power density, a fast charge–discharge rate and a long life span. Therefore, the electrochemical performances of C₆₀/NFO/HE-LVP/SC were significantly improved via the synergistic effects of different components and different charge storage mechanisms.

Experimental procedures

Preparation of C₆₀/NFO/HE-LVP/SC

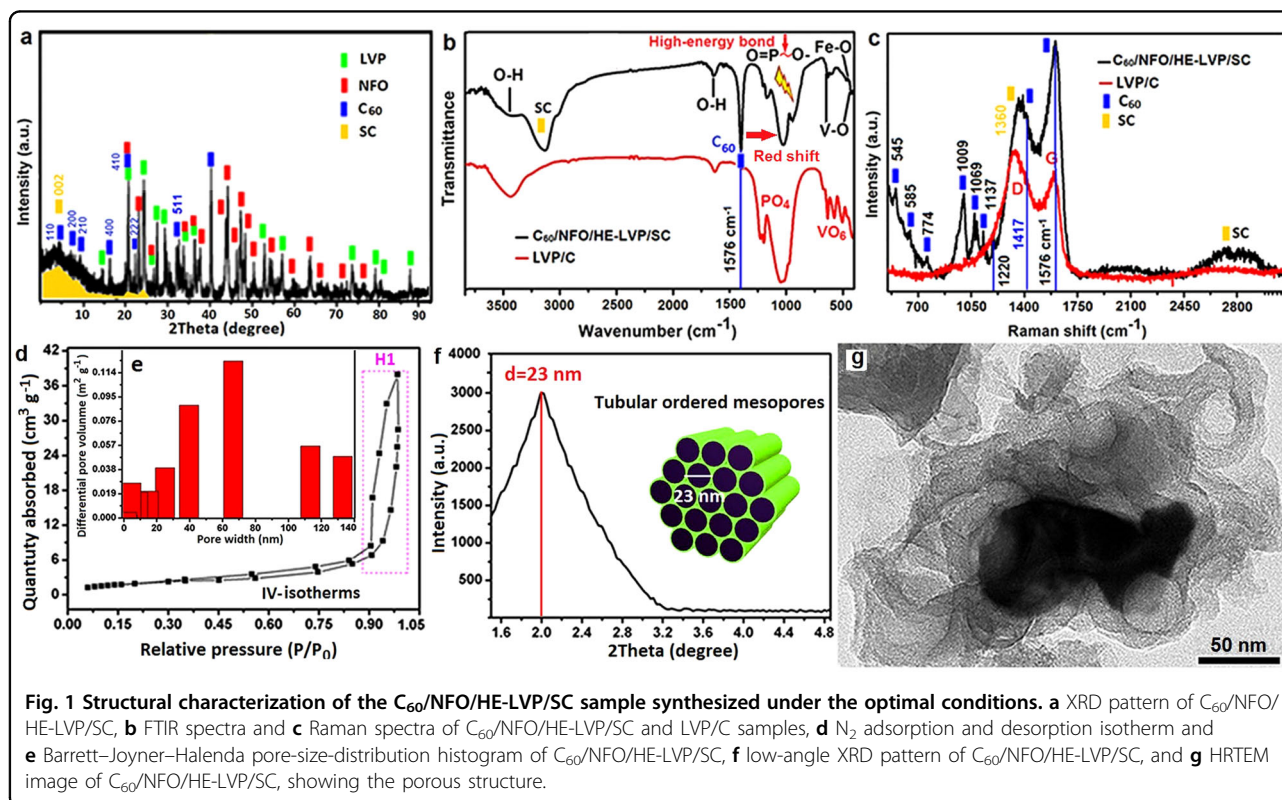
C₆₀/NFO/HE-LVP/SC was prepared using an Na₂ATP high-energy biotemplate, the freeze-drying technique and the carbon thermal reduction method. The detailed fabrication of C₆₀/NFO/HE-LVP/SC is schematically illustrated in Figure S1 (Supporting Information). First, FeCl₃ solution was added to Na₂ATP solution after incubation to form NaFe-ATP sediment. Second, NaFe-ATP sediment after washing and drying was mixed with (NH₄)₂HPO₄ and NH₄VO₃ solutions in a molar ratio of $n_{\text{Fe}}:n_{\text{V}} = 1:x$ ($x = 1/3, 1/2, 1, 2, 3$) and $n_{\text{V}}:n_{\text{P}} = 2:3$ for 12 h to form a NaFeVP-ATP sediment precursor. Third, NaFeVPO₄-ATP precursors were dried through freeze drying at -50 °C and dried in an oven at 80 °C. Subsequently, the dry Na-FeVPO₄-ATP mixtures were mixed with Li₂CO₃ and glucose in a molar ratio of $n_{\text{Li}}:n_{\text{V}}:n_{\text{G}} = 3:2:0.25$ for 2 h through a dry ball-milling process. Finally, the resulting mixtures were annealed at 600/700/800 °C for 8 h.

Material characterizations

See Supporting Information S3.

Electrode fabrication and testing

The hybrid devices were assembled in the form of CR 2032 coin cells in an argon-filled glove box, where lithium metal foil was used as the counter and reference electrodes, and polypropylene film was used as a separator. A Li⁺ electrolyte and a Na⁺ electrolyte in a volume ratio of 1:1 were used as a Li⁺/Na⁺ mixed-ion electrolyte. The Li⁺ electrolyte consisted of 1 M LiPF₆ and ethylene carbonate/dimethyl carbonate/ethylene methyl carbonate in a volume ratio of 1:1:1 (1 M LiPF₆/EC/DEC/EMC electrolyte). The Na⁺ electrolyte was composed of 1 M NaClO₄ and propylene carbonate (1 M NaClO₄/PC). For fabrication of the C₆₀/NFO/HE-LVP/SC hybrid electrode, 80 wt% active material, 10 wt% acetylene black conducting agent and 10 wt% poly(vinylidene fluoride) binder were mixed in N-methyl pyrrolidinone. Then, the mixture slurry was uniformly spread on an aluminum foil and dried in air atmosphere at 60 °C for 5 h and in vacuum at 120 °C for 10 h. Electrodes with mass loading of C₆₀/NFO/HE-LVP/SC ranging from 0.9 to 1.8 mg cm⁻² were punched in a form 15 mm in diameter. Assembly of the hybrid devices was carried out in an argon-filled glove box. Cyclic voltammetry (CV) and electrochemical impedance spectroscopy (EIS) measurements were performed on a



PARSTAT 2263 electrochemical workstation. The EIS spectra were recorded for frequencies ranging from 100 kHz to 10 MHz. The voltage range of CV measurements was 2.5–4.2 V, and the scan rate was from 0.1 to 4.0 mV s⁻¹. All tests were performed at room temperature.

Results and discussion

Characterizations of the morphology and structure

To investigate the structure of the synthesized samples, X-ray diffraction (XRD), Fourier transform infrared spectroscopy (FTIR) and Raman spectroscopy were performed, as shown in Fig. 1. The diffraction peaks of the C₆₀/NFO/HE-LVP/SC sample in Fig. 1a are indexed to Li₃V₂(PO₄)₃ (LVP) (JCPDS no. 47-0107), Na₄FeO₃ (NFO) (JCPDS no. 34-0891), and C₆₀ (JCPDS no. 49-1720). There is a small broad bump in the low-angle 2θ range from 2 to 25°, corresponding to the (002) plane of soft carbon (SC) with a low degree of order¹². The results calculated using Jade 5 XRD pattern-processing software show that the C₆₀/NFO/HE-LVP/SC sample synthesized at 700 °C has smaller primary crystallite size and strain (Table S2). The primary crystallite sizes of LVP and NFO in C₆₀/NFO/HE-LVP/SC are 51.7 and 26.9 nm, respectively. The strains of LVP and NFO in C₆₀/NFO/HE-LVP/SC are 0.16% and 0.13%, respectively. These results indicate that the crystal structure features of LVP and NFO in the samples synthesized at different temperatures can be controlled by adjusting the synthesis temperature.

To characterize the formation of high-energy Li₃V₂(PO₄)₃ and C₆₀ nanocages, the FTIR spectra of the C₆₀/NFO/HE-LVP/SC and LVP/C samples are shown in Fig. 1b. In Fig. 1b, the infrared characteristic absorbing bands in the range of 400–700 cm⁻¹, 900–1300 cm⁻¹ and 3300–3600 cm⁻¹ correspond to the Fe–O, V–O, PO₄ and O–H bands. The infrared spectral bands of the LVP/C sample are mainly distributed over two wavenumber ranges from 460 to 750 cm⁻¹ and 940 to 1280 cm⁻¹. The dominant bands from 940 to 1280 cm⁻¹ are due to the internal stretching, internal bending and external oscillation modes of PO₄³⁻. The bands from 460 to 750 cm⁻¹ correspond to the intramolecular symmetrical stretching vibrations of the V–O bond in the VO₆ unit.

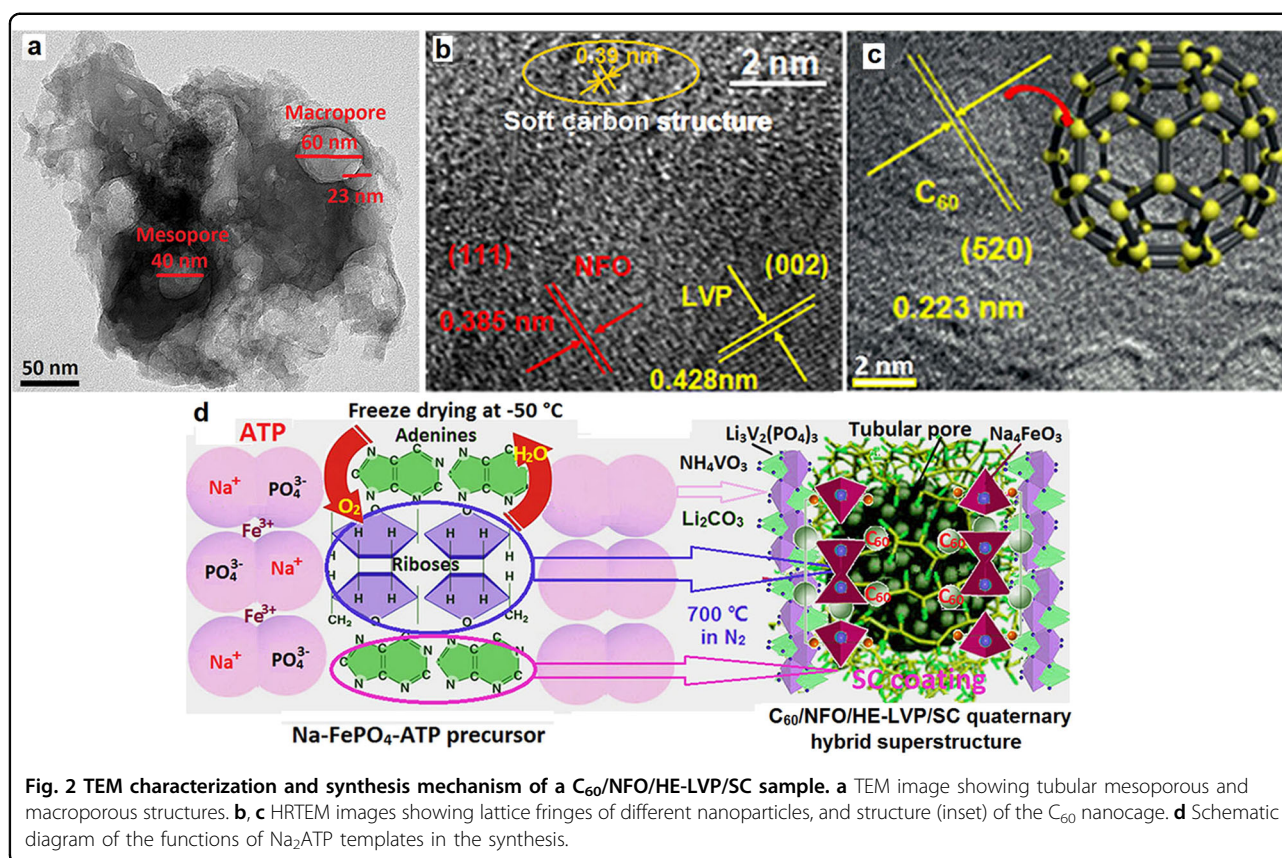
According to Hooke's law, the wavenumber (σ) of PO₄³⁻ bands can be calculated using the following equation:

$$\sigma = 1303 \sqrt{\frac{k}{\mu}} \quad (1)$$

where k and μ represent the bond force constant and atomic reduced mass, respectively. By comparing the FTIR spectra of the C₆₀/NFO/HE-LVP/SC and LVP/C samples, three main changes are observed in the FTIR spectrum of the C₆₀/NFO/HE-LVP/SC sample. First, all

the PO₄³⁻ bands have shifted to lower wavenumbers (redshift) relative to those of the LVP/C sample (red arrow in Fig. 1b), which means that k is reduced, and the P–O chemical bond length increases. Second, a new band at 938 cm⁻¹ was formed in the FTIR spectrum of the C₆₀/NFO/HE-LVP/SC sample, which indicates that high-energy phosphate bonds have been introduced into LVP (yellow arrow in Fig. 1b). Third, the vibration transmittance of the PO₄³⁻ and V–O bands was weakened in the FTIR spectrum of the C₆₀/NFO/HE-LVP/SC sample. These changes indicate that there are some interactions between the NFO and high-energy LVP nanoparticles within the mesoporous carbon network. The sharp and strong band at 1576 cm⁻¹ is characteristic of pristine C₆₀, further confirming the existence of molecular C₆₀⁵². The wide and strong band in the range of 2850–3250 cm⁻¹ is characteristic of SC, which is mutually complementary to the Raman spectrum in Fig. 1c.

The Raman spectra of both the C₆₀/NFO/HE-LVP/SC and LVP/C samples in Fig. 1c reveal two characteristic peaks located at approximately 1369 and 1576 cm⁻¹ that are attributed to the D-band (representing the disordered carbon structure) and G-band (representing the ordered carbon structure), respectively. The Raman spectrum of the C₆₀/NFO/HE-LVP/SC sample is clearly different from that of the LVP/C sample. The relative peak intensity ratio (I_G/I_D) of the G-band and the D-band can be used to estimate the ordered degree of the carbon structure. The I_G/I_D of the C₆₀/NFO/HE-LVP/SC and LVP/C samples are 1.24 and 0.89, respectively, which indicates that the carbon formed by the pyrolysis and carbonization of Na₂ATP biotemplates in the C₆₀/NFO/HE-LVP/SC sample retains high crystallinity and ordered degree. The Raman spectrum of the C₆₀/NFO/HE-LVP/SC sample has characteristic peaks for pristine C₆₀, corresponding to the typical Ag (at 545 and 1417 cm⁻¹) and Hg (at 585, 774, 1009, 1069, 1137, 1220, and 1576 cm⁻¹) vibrational modes. The peak from the Ag 'pentagonal pinch' mode is located at 1417 cm⁻¹, which is known to be sensitive to the intermolecular bonding. The wide and strong band at 1360 cm⁻¹ and the wide band in the range of 2750–2950 cm⁻¹ are characteristics of SC, which is consistent with the FTIR spectrum results in Fig. 1b. The Raman spectrum of the C₆₀/NFO/HE-LVP/SC sample has characteristic peaks for pristine C₆₀ and SC⁵³. The Raman and FTIR spectra results unequivocally confirm that the carbon is in the forms of C₆₀ and SC in the C₆₀/NFO/HE-LVP/SC sample, which is also validated by the HRTEM images in Fig. 2b, c. These results show that the C₆₀/NFO/HE-LVP/SC sample is composed of NFO, LVP, C₆₀ and SC. The C₆₀ nanocages and SC were formed by the pyrolytic carbonization of the high-energy biotemplate (Na₂ATP) during the synthesis (Fig. 2d). The carbon content



measured with an elemental analyzer is 7.48%. To determine the crystal phase contents of the C_{60} /NFO/HE-LVP/SC sample, quantitative analysis was performed with a Shimadzu XRD-700 X-ray diffractometer (P/N305-20256-01). The analysis results show that the C_{60} /NFO/HE-LVP/SC sample contains 60.83% HE-LVP nanocrystals and 31.69% NFO nanocrystals.

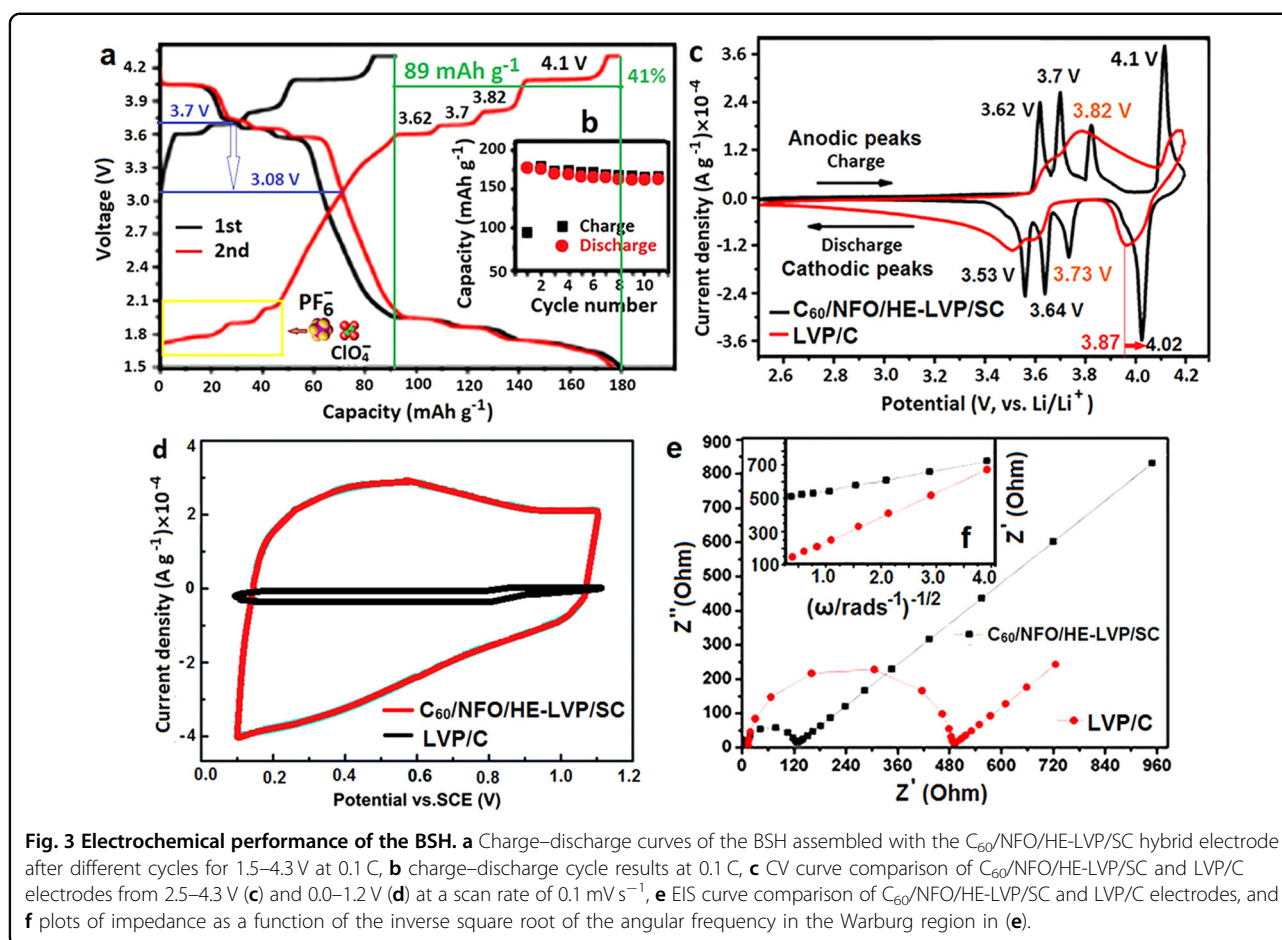
The morphology and tubular ordered mesoporous superstructure of the C_{60} /NFO/HE-LVP/SC sample were inspected and confirmed by means of high-resolution transmission electron microscopy (HRTEM), low-angle X-ray diffraction (SAXRD, 2θ range of $1.5\text{--}5.0^\circ$) and surface area analysis. The N_2 adsorption–desorption isotherm of the C_{60} /NFO/HE-LVP/SC sample (Fig. 1d) shows a type-IV adsorption isotherm and an H1 hysteresis loop in the relative pressure (P/P_0) range of 0.85–0.95, suggesting a typical ordered mesoporous feature caused by simple cylindrical connecting pores⁵⁴. The Barrett–Joyner–Halenda pore-size-distribution histogram in Fig. 1e indicates that the C_{60} /NFO/HE-LVP/SC sample has a hierarchical pore structure, and the pore-size distribution ranges from 2 to 132 nm. The TEM images in Figs. 1g, 2a also show that the sample has tubular porous channels of different sizes, such as 40 and 60 nm. The SAXRD pattern in Fig. 1f indicates that the sizes of the highly ordered mesoporous cylindrical channels are

centered around 23 nm, as calculated by the Bragg equation (see Supplementary Eq. S1).

The TEM images in Figure S1a–c show some layered particles and a single particle with mesopores (5–50 nm) (Figure S1c) in the C_{60} /NFO/HE-LVP/SC sample. In Fig. 2b and Figure S1f, the HRTEM images of the C_{60} /NFO/HE-LVP/SC sample show the clear crystal fringes of NFO and LVP. The lattice fringes with spacings of 0.385 and 0.428 nm are indexed to the (111) facet of NFO and (002) facet of LVP, respectively. Figure 2c shows the crystal fringes of C_{60} , which corroborates the XRD (Fig. 1a) and Raman (Fig. 1c) measurement results. Figure 2b and Figure S1d also reveal that the SC consists of two separated backbones (with a spacing of ~ 0.39 nm between them), and the two backbones are densely connected via many streaks. The HRTEM images show that the diameter of the C_{60} nanocage is $\sim 1\text{--}2$ nm (Figure S1ef). In principle, the cross-linked backbones could provide a stable framework and electron transport channels, while the porous structure would promote infiltration of the electrolyte into the SC and accommodate the volume expansion^{55,56}.

Synthesis mechanism

These results show that the successful formation of the C_{60} /NFO/HE-LVP/SC superstructure with tubular



ordered mesopores is due to the self-assembly function of the Na_2ATP high-energy biotemplate and the optimization of the freeze-drying parameters. The freeze-drying (or lyophilization) technique can be used to create a complex scaffold with a controlled, porous architecture⁵⁷. Figure 2d shows a schematic diagram of the role of Na_2ATP in the formation of hierarchical ordered mesoporous superstructure frameworks. In the synthesis, high-energy Na_2ATP biomolecules self-assemble due to the hydrophobic effect, resulting in the formation of spherical micelles with negative charges. When the Fe^{3+} solution is added to the Na_2ATP micelle solution, the positively charged iron ions can preferentially combine the high-energy phosphorous groups with negative charges in the Na_2ATP micelle particles via electrostatic interactions, leading to the formation of the $Na-FePO_4-ATP$ precursor. In the freeze drying at $-50\text{ }^\circ\text{C}$, the hydrophilic ribose units in the micelles are easily oxidized and dehydrated, and the frozen water in the micelles directly sublimates to the gas phase via reduction of the surrounding pressure (28 Pa) to form an ordered mesoporous superstructure. The hydrophobic adenine units and hydrophilic ribose units in the micelles are transformed into a soft carbon coating

and C_{60} at $700\text{ }^\circ\text{C}$, respectively. In addition, there are high-energy phosphorus bonds in the Na_2ATP micelles, which can be used as a phosphorus source and a nucleating agent of $Li_3V_2(PO_4)_3$ during the synthesis. Therefore, the Na_2ATP high-energy biotemplate plays a key role in the formation of $C_{60}/NFO/HE-LVP/SC$. Such a tubular ordered mesoporous superstructure can not only improve the transfer kinetics of the electrolyte but also facilitate anion insertion, providing a short diffusion path for mass and charge transport. This superstructure was built with different nanoparticles, such as C_{60} nanocages, NFO, HE-LVP, and SC, forming a three-dimensional ordered mesoporous structure.

Electrochemical characterizations

The electrochemical performances of the BSH assembled with the $C_{60}/NFO/HE-LVP/SC$ hybrid electrode as the cathode and Li metal as the anode were investigated in a Li/Na mixed electrolyte over a potential range of 0.01–4.3 V, as shown in Fig. 3. The first discharge capacity (108.1 mAh g^{-1}) of the $C_{60}/NFO/HE-LVP/SC$ hybrid electrode is higher than that (97.5 mAh g^{-1}) of the LVP/C electrode at 0.1 C in a potential window of 2.5–4.2 V

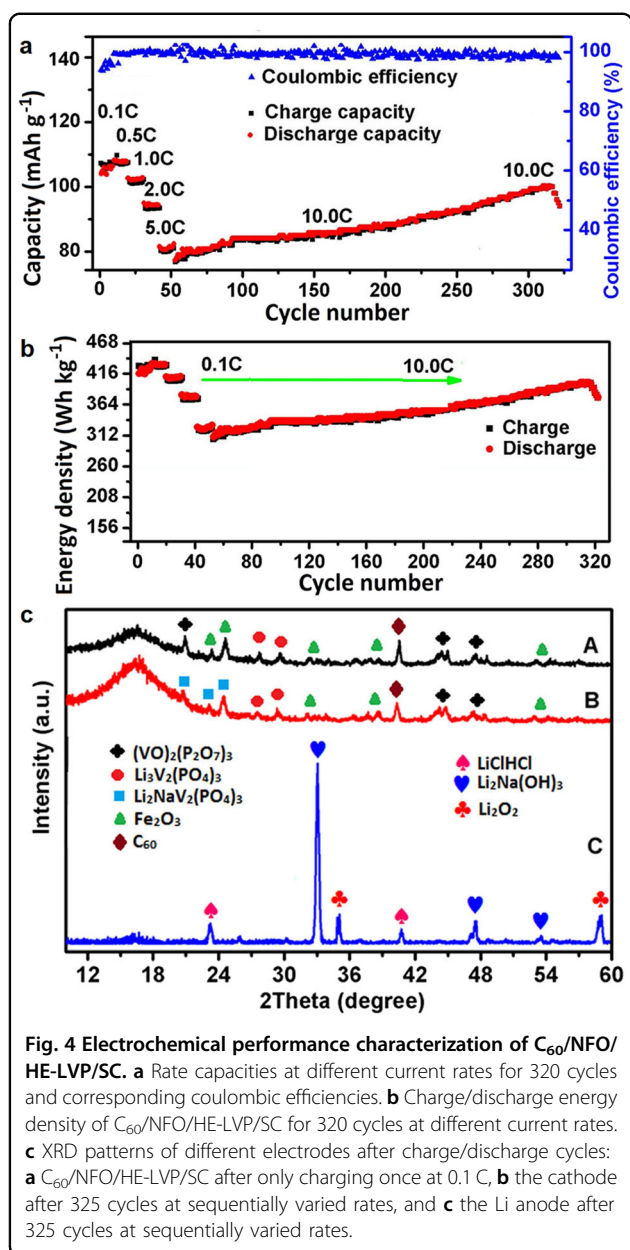
(Figure S2a). There are four distinct plateaus (3.62/3.53, 3.7/3.64, 3.82/3.73, and 4.1/4.02 V) in the charge/discharge curves of $C_{60}/\text{NFO}/\text{HE-LVP}/\text{SC}$, while LVP/C has only three plateaus (3.65/3.53, 3.78/3.60, and 4.16/3.87 V). Obviously, NFO in the $C_{60}/\text{NFO}/\text{HE-LVP}/\text{SC}$ hybrid electrode can reversibly release and uptake sodium ions at the plateaus of 3.82/3.73 V, which provides an $\sim 14\%$ extra capacity (Figure S3a). This gain is related to the iron redox couple of $\text{Fe}^{2+}/\text{Fe}^{3+}$. Figure 3a shows the galvanostatic charge–discharge curves of the $C_{60}/\text{NFO}/\text{HE-LVP}/\text{SC}$ hybrid electrode at a current density of 0.1 C over a wide voltage range (1.5–4.3 V), exhibiting a discharge capacity of 180 mAh g^{-1} for two cycles. These results show that Li and Na ions can be inserted into HE-LVP and NFO, endowing $C_{60}/\text{NFO}/\text{HE-LVP}/\text{SC}$ with a high capacity due to the multiple redox couples of $\text{V}^{3+}/\text{V}^{4+}$ and $\text{Fe}^{2+}/\text{Fe}^{3+}$, which clearly surpasses the theoretical capacity of LVP (137 mAh g^{-1}). The charge/discharge curve (red line) after two cycles is clearly different from the first charge–discharge curve, showing a typical profile of anion intercalation/deintercalation into/from $C_{60}/\text{NFO}/\text{HE-LVP}/\text{SC}$. First, the intersection voltage of the charge and discharge curves after 2 cycles has been reduced from 3.7 to 3.08 V, and the charge capacity exhibits a 41% increase ($\sim 89 \text{ mAh g}^{-1}$). This may be attributed to the extra charge storage mechanism. Second, the three small charge voltage plateaus in the low voltage range (1.5–1.95 V) correspond to $\text{PF}_6^-/\text{ClO}_4^-$ anion intercalation in the tubular ordered mesoporous structure (shown in Fig. 5b later).

The different charge storage mechanisms of the $C_{60}/\text{NFO}/\text{HE-LVP}/\text{SC}$ hybrid electrode can be proposed based on the cyclic voltammetry (CV) results through appropriate experimental design. Figure 3b shows the difference in the CV curves of $C_{60}/\text{NFO}/\text{HE-LVP}/\text{SC}$ and LVP/C in the voltage range of 2.5–4.3 V at a scan rate of 0.1 mV/s. When LVP/C was used as the electrode, it showed three pairs of redox peaks (3.65/3.53, 3.78/3.60, and 4.16/3.87 V) similar to pure LVP. This can be ascribed to the intercalation and deintercalation of Li^+ ions into and from the LVP lattice, accompanied by the electrochemical conversion of V^{3+} to various valence states. The LVP/C electrode only shows a typical battery-like behavior, so its total charge mainly comes from the diffusion-controlled process. In the CV curve of $C_{60}/\text{NFO}/\text{HE-LVP}/\text{SC}$, the HE-LVP not only exhibits well-separated redox peaks (3.62/3.53, 3.7/3.64, and 4.1/4.02 V) but also has a higher current intensity of the peaks than that of LVP/C, especially in the high voltage range (3.9–4.2 V). The NFO has one pair of smaller charge/discharge voltage peaks (3.82/3.73 V) for the redox of $\text{Fe}^{2+}/\text{Fe}^{3+}$ vs. Na^+/Na . In particular, when the scan rate is increased, the intensity of all redox peaks gradually increases (Figure S4d). When the scan rate is increased to 1.0 mV s^{-1} , the four anodic peaks merge into the three wide bumps (Figure S6c), and the

anodic peak at 4.1 V has a tendency to disappear with increasing sweep rate (Figure S6d–f), verifying the transition from battery-type to pseudocapacitive behavior⁵. The pseudocapacitive contribution dominates the total charge storage at high sweep rates of $1.5\text{--}2.5 \text{ mV s}^{-1}$ (Figure S6d–f)⁷. This is due to the emergence of extrinsic faradaic reactions in C_{60} with high electrical conductivity and electroactive NFO that replace the diffusion-controlled lithium ion interactions in HE-LVP⁷. C_{60} and NFO mainly contribute to intercalation pseudocapacitive and redox pseudocapacitive charge storage, respectively (Figure S7). Therefore, $C_{60}/\text{NFO}/\text{HE-LVP}/\text{SC}$ exhibits fast charge-transfer kinetics and a superior rate performance by maximizing the coupling effects of the individual components. To obtain further insight into the evolution of anion extraction/insertion, the CV curves of $C_{60}/\text{NFO}/\text{HE-LVP}/\text{SC}$ and LVP/C were measured in the low voltage range (0–1.2 V) (Fig. 3d). $C_{60}/\text{NFO}/\text{HE-LVP}/\text{SC}$ exhibits a nearly rectangular CV curve without distinct redox peaks, showing electrochemical behavior similar to that of electric double layer (EDL) capacitors. This is the characteristic of a surface-confined charge-transfer process, verifying that $C_{60}/\text{NFO}/\text{HE-LVP}/\text{SC}$ also possesses an EDL mechanism of surface-controlled processes because $\text{PF}_6^-/\text{ClO}_4^-$ anions can be easily intercalated into the EDL of the tubular ordered mesopores (Fig. 5b). In contrast, the CV curve of LVP/C exhibits a nonrectangular shape at the same scan rate, indicating reversible faradaic reactions.

Figure 3e shows EIS curves for comparison of the $C_{60}/\text{NFO}/\text{HE-LVP}/\text{SC}$ and LVP/C electrodes. The charge-transfer resistance (semicircle diameter, $R_{\text{ct}} = 127.5 \Omega$) of the $C_{60}/\text{NFO}/\text{HE-LVP}/\text{SC}$ hybrid electrode is far less than that ($R_{\text{ct}} = 491.8 \Omega$) of LVP/C. Figure 3f shows that $C_{60}/\text{NFO}/\text{HE-LVP}/\text{SC}$ has a higher ion diffusion coefficient ($D = 8.9 \times 10^{-3} \text{ cm}^2 \text{ s}^{-1}$) than that ($D = 6.2 \times 10^{-4} \text{ cm}^2 \text{ s}^{-1}$) of LVP/C (Table S2). The results indicate that the $C_{60}/\text{NFO}/\text{HE-LVP}/\text{SC}$ hybrid electrode accelerates the movement of mixed ions and improves the rate performance. Although the capacity of $C_{60}/\text{NFO}/\text{HE-LVP}/\text{SC}$ gradually decreases with increasing current rate (Figure S2b), it still exhibits a capacity of $\sim 77.3 \text{ mAh g}^{-1}$ and an ultrahigh coulombic efficiency of 100% at a high current rate of 10 C (Fig. 4a), indicating its ultrafast kinetics. Interestingly, its capacity gradually increases with cycle number from 50 to 300 cycles at 10 C. The capacity reaches 98.4 mAh g^{-1} , and an ultrahigh capacity retention of 204.2% is obtained.

The energy density values E (Wh kg^{-1}) of the $C_{60}/\text{NFO}/\text{HE-LVP}/\text{SC}$ and LVP/C electrodes were obtained by galvanostatic charge–discharge measurements. The power density values P (W kg^{-1}) of $C_{60}/\text{NFO}/\text{HE-LVP}/\text{SC}$ and LVP/C were calculated by Supplementary Eq. S2. Figure S2c shows that both the energy density and power density of $C_{60}/\text{NFO}/\text{HE-LVP}/\text{SC}$ are much higher than



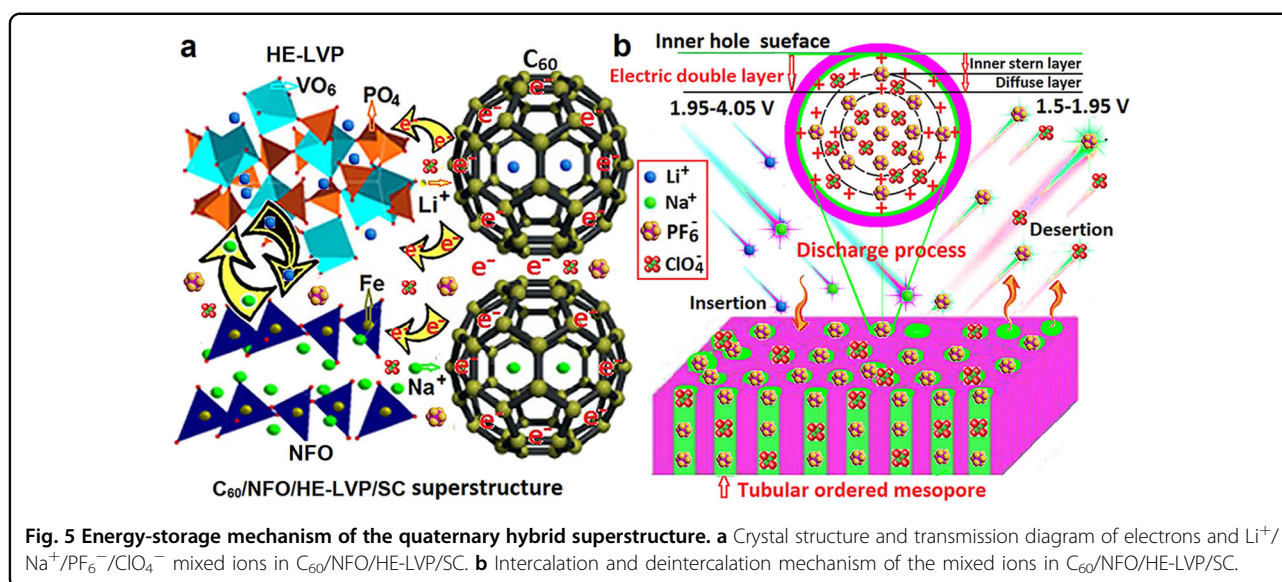
those of LVP/C. The C_{60} /NFO/HE-LVP/SC hybrid electrode not only exhibits an ultrahigh energy density of 405 Wh kg^{-1} and a high power density of 413 W kg^{-1} but also delivers superb cycling stability (with an energy retention of 135%) after 300 cycles at 10.0 C (Fig. 4b). To the best of our knowledge, such energy density and power capability even exceed the results for all Li-ion and Na-ion BSHs reported thus far (Table S1). The results show that the reversible multielectron reactions (see Supplementary Eqs. S3–8) of HE-LVP and NFO can achieve a high energy density. Therefore, C_{60} /NFO/HE-LVP/SC realizes high rate insertion and extraction of mixed ions and improvement of the rate performance and energy density.

To the best of our knowledge, this is the first report of quaternary hybrid electrodes with such excellent performance in terms of ultrahigh energy density. To prove the electrode reactions and structural changes, we performed XRD analysis of electrodes after charge/discharge cycles, as shown in Fig. 4c. The results indicate that Na^+ can participate in ionic exchange, C_{60} nanocages transfer electrons and fixate the electrolyte, and Na^+ can be deposited on the surface of the Li anode (see Supplementary Information S6 for details).

The electrochemical performances of different electrodes synthesized under different conditions (molar ratio of V/Fe, heat treatment temperature and drying method) were evaluated and compared based on charge/discharge tests using CR 2032 coin cells (Figure S4a–c) and thermogravimetric analysis (TGA) (Figure S5). We found that the optimal molar ratio of V:Fe is 1:1 (Figure S4a), the optimal heat treatment temperature is 700°C (Figure S4b) and the optimal drying method is freeze drying (Figure S4c). The electrochemical kinetics of C_{60} /NFO/HE-LVP/SC was investigated by EIS measurements. Figure S4ef shows that the R_{ct} and D values of C_{60} /NFO/HE-LVP/SC change slightly after 10 CV cycles at the scan rates of $0.1\text{--}0.5 \text{ mV s}^{-1}$ (Table S3). However, the R_{ct} and D values are almost unchanged after 10 CV cycles at the high scan rates of $1.0\text{--}4.0 \text{ mV s}^{-1}$, which further confirms that C_{60} /NFO/HE-LVP/SC has outstanding reversibility and cycling stability of mixed-ion extraction/insertion reactions.

Based on the CV measurements (Figures S4 and S6), the C_{60} /NFO/HE-LVP/SC hybrid electrode possesses hybrid energy-storage mechanisms, including Li^+/Na^+ intercalation pseudocapacitance in C_{60} , Na^+ redox pseudocapacitance in NFO, Li^+ diffusion in the crystal framework of HE-LVP and $\text{PF}_6^-/\text{ClO}_4^-$ anion intercalation in the tubular ordered mesoporous structure (Figure S7). In the tubular ordered mesoporous structure, energy is stored via adsorption and electrostatic accumulation of charges on the electrode–electrolyte interface without any faradaic reactions, leading to a high power density, a fast charge–discharge rate and a long life span⁷. In the case of the battery-type behavior of HE-LVP, energy is stored via the reversible redox reactions (faradaic reactions) with bulk phase transformation upon charging/discharging, providing high energy density and cyclability. In addition, C_{60} and NFO are also good electroactive materials that provide an extra pseudocapacitance, a high conductivity and mechanical stability. Therefore, the electrochemical performances of C_{60} /NFO/HE-LVP/SC are significantly increased by the synergistic effects of different components.

Figure 5a shows the crystal structure, the Li^+/Na^+ ion exchange occurring between HE-LVP and NFO, and the transfer diagram of electrons and $\text{Li}^+/\text{Na}^+/\text{PF}_6^-/\text{ClO}_4^-$



mixed ions in C₆₀/NFO/HE-LVP/SC. The superior electrochemical performances of C₆₀/NFO/HE-LVP/SC can be attributed to the collective and synergetic effects of the multicomponents, nanostructures and energy-storage mechanisms. First, different nanoparticles can provide a high ion storage interface and efficient electron/ion transport pathways for fast ion intercalation. Second, the tubular ordered mesopores not only provide a large electrode/electrolyte interface area but also adsorb PF₆⁻ and ClO₄⁻ anions from the electrolyte, which allows ultrafast electrolyte ion uptake into or removal from C₆₀/NFO/HE-LVP/SC through a short diffusion pathway. C₆₀ nanocages can rapidly transfer electrons since π -bonds and the nanocage structure are open for electrons. Figure 5b shows that an electric double layer (EDL) can form on the inner surface of tubular ordered mesopores in C₆₀/NFO/HE-LVP/SC, and its surface curvature is an important factor in promoting the adsorption of the anions in the electrolyte. The anions can be bound to the porous inner Stern layer of the EDL and stabilized by the positively charged surface of the porous wall via electrostatic interaction. The outer diffuse layer of the EDL is composed of mobile anions, and their distribution depends on the electrostatic interaction. The formation mechanism of the EDL inside the tubular ordered mesopores is proposed as follows: First, there are many positively charged ionic groups in the network structure of C₆₀/NFO/HE-LVP/SC. Li⁺ and Na⁺ in the C₆₀/NFO/HE-LVP/SC framework enter the inner layer of the EDL, positively charging the inner layer, which can adsorb and immobilize PF₆⁻ and ClO₄⁻ anions in the electrolyte to form the EDL. Second, the negative curvature of the tubular ordered mesopores can improve the adsorption of the anions on the inner Stern layer, increase the number

of insertion sites of hybrid ions and enhance the electrochemical performance. In the inner layer of the EDL, the concentration of hybrid ions is higher than that in the bulk, leading to strong adsorption and high ionic activity. As stated above, the EDL theory could explain the high number of insertion sites of hybrid ions inside the tubular ordered mesopores of C₆₀/NFO/HE-LVP/SC. More importantly, the C₆₀ with the cage-like structure and soft carbon in C₆₀/NFO/HE-LVP/SC also play important roles in enhancing the electrochemical performance. In the discharge process, not only do Na⁺/Li⁺ ions in the electrolyte intercalate into the different nanoparticles between 1.95 and 4.05 V, which corresponds to the electrochemical energy-storage mechanisms (faradaic) with phase changes and redox reactions, but also, PF₆⁻/ClO₄⁻ anions deintercalate from the diffuse layer of the tubular ordered mesopores at the low current rates (0.1–5 C) between 1.5 and 1.95 V, which is based on the electrophysical energy-storage mechanism (non-faradaic) of the EDL⁷. However, the PF₆⁻/ClO₄⁻ anions begin to deintercalate from the inner Stern layer of the tubular ordered mesopores at a high current rate of 10 C, which leads to an ultrahigh capacity retention of 204.2% from 50 to 300 cycles. Due to the collective and synergetic effects of different nanoparticles, C₆₀ nanocages and tubular ordered mesopores, the C₆₀/NFO/HE-LVP/SC hybrid electrode utilizes hybrid energy-storage mechanisms, exhibiting an ultrahigh energy density and excellent rate capability and cycling stability¹.

Conclusion

In summary, we have synthesized a quaternary hybrid superstructured material using a high-energy biotemplate as sodium, phosphorus and carbon sources via the freeze-drying technique and carbon thermal reduction

method. This material is composed of highly stable fullerene C_{60} nanocages (~ 2 nm), Na_4FeO_3 (NFO), high-energy $Li_3V_2(PO_4)_3$ (HE-LVP), soft carbon (SC) and a tubular ordered mesoporous structure. The C_{60} nanocages not only possess high conductivity and degree of crystallinity but also show an extra Li^+ intercalation pseudocapacitance. These different nanoparticles as building blocks with fully exposed active edges are oriented in a preferred manner, which benefits the excellent electrochemical performance. As a quaternary hybrid electrode material for BSHs, C_{60} /NFO/HE-LVP/SC exhibits some new electrochemical performances, such as a capacity self-enhancement performance, an ultrahigh capacity retention of 204.2% and an ultrahigh energy density of 405 Wh kg^{-1} (power density of 413 W kg^{-1}) after 300 cycles at 10.0 C , because of the hybrid energy-storage mechanisms. Furthermore, C_{60} /NFO/HE-LVP/SC has electrochemically active redox reactions of Fe^{2+}/Fe^{3+} and V^{3+}/V^{4+} and exhibits a coulombic efficiency of $\sim 100\%$. We hope that this work can demonstrate that the energy density can be largely improved via the design of a unique hybrid superstructure, which provides new insights for realizing high-performance BSHs.

Acknowledgements

The authors thank the National Natural Science Foundation of China (Grant Nos. 51672139, 51472127, 51272144, and 51702177) for the financial support. Open access funding provided by Uppsala University.

Author details

¹Institute of Materials Science and Engineering, Qilu University of Technology (Shandong Academy of Sciences), Jinan 250353, China. ²Institute of Materials Science and Engineering, Shandong University of Science and Technology, Qingdao 266590, China. ³Department of Chemistry - Ångström Laboratory, Uppsala University, Box 538, SE-75121 Uppsala, Sweden

Authors contributions

X.Z., W.H., and J.Z. conceived the research and designed the work. X.X. performed the synthesis, characterization and electrochemical measurements of the materials. Y.H. coordinated the experimental work. G.X. performed HRTEM and FTIR spectroscopy experiments. X.Z., W.H., and J.Z. edited and finalized the paper. All authors discussed the results and commented on the paper.

Conflict of interest

The authors declare that they have no conflict of interest.

Publisher's note

Springer Nature remains neutral with regard to jurisdictional claims in published maps and institutional affiliations.

Supplementary information is available for this paper at <https://doi.org/10.1038/s41427-019-0189-8>.

Received: 20 September 2019 Revised: 16 November 2019 Accepted: 20 November 2019.

Published online: 24 January 2020

References

- Kuno, M. et al. A quantitative and spatially resolved analysis of the performance-bottleneck in high efficiency, planar hybrid perovskite solar cells. *Energy Environ. Sci.* **11**, 960–969 (2018).
- Lukatskaya, M. R., Dunn, B. & Gogotsi, Y. Multidimensional materials and device architectures for future hybrid energy storage. *Nat. Commun.* **7**, 12647 (2016).
- Zhu, X., Sun, D., Luo, B., Hu, Y. & Wang, L. A stable high-power $Na_2Ti_3O_7/LiNi_{0.5}Mn_{1.5}O_4$ Li-ion hybrid energy storage device. *Electrochim. Acta* **284**, 30–37 (2018).
- Jo, C. H. et al. Bioinspired surface layer for the cathode material of high-energy-density sodium-ion batteries. *Adv. Energy Mater.* **8**, 1702942 (2018).
- Jo, C. H., Choi, J. U., Yashiro, H. & Myung, S. T. Controllable charge capacity using a black additive for high-energy-density sodium-ion batteries. *J. Mater. Chem. A* **7**, 3903–3909 (2019).
- Zuo, W. et al. Battery-supercapacitor hybrid devices: recent progress and future prospects. *Adv. Sci.* **4**, 1600539 (2017).
- Liu, J. et al. Advanced energy storage devices: basic principles, analytical methods, and rational materials design. *Adv. Sci.* **5**, 1700322 (2018).
- Zhang, X., Tang, Y., Zhang, F. & Lee, C.-S. A novel aluminum–graphite dual-ion battery. *Adv. Energy Mater.* **6**, 1–6 (2016).
- Tong, X., Zhang, F., Ji, B., Sheng, M. & Tang, Y. Carbon-coated porous aluminum foil anode for high-rate, long-term cycling stability, and high energy density dual-ion batteries. *Adv. Mater.* **28**, 9979–9985 (2016).
- Nakano, H. et al. Anion secondary batteries utilizing a reversible BF_4 insertion/extraction two-dimensional Si material. *J. Mater. Chem. A* **2**, 7588–7592 (2014).
- Li, J., Ma, C., Chi, M., Liang, C. & Dudney, N. J. Solid electrolyte: the key for high-voltage lithium batteries. *Adv. Energy Mater.* **5**, 1401408 (2015).
- Xu, K. Electrolytes and interphases in Li-ion batteries and beyond. *Chem. Rev.* **114**, 11503–11618 (2014).
- Hou, Y., Cheng, Y., Hobson, T. & Liu, J. Design and synthesis of hierarchical MnO_2 nanospheres/carbon nanotubes/conducting polymer ternary composite for high performance electrochemical electrodes. *Nano Lett.* **10**, 2727 (2010).
- Chen, Z. et al. High-performance sodium-ion pseudocapacitors based on hierarchically porous nanowire composites. *ACS Nano* **6**, 4319–4327 (2012).
- Yan, W. et al. Lithographically patterned gold/manganese dioxide core/shell nanowires for high capacity, high rate, and high cyclability hybrid electrical energy storage. *Chem. Mater.* **24**, 2382–2390 (2012).
- Guan, D., Gao, X., Li, J. & Yuan, C. Enhanced capacitive performance of TiO_2 nanotubes with molybdenum oxide coating. *Appl. Surf. Sci.* **300**, 165–170 (2014).
- Qian, T. et al. Interconnected three-dimensional V_2O_5 /polypyrrole network nanostructures for high performance solid-state supercapacitors. *J. Mater. Chem. A* **3**, 488–493 (2015).
- Yu, G. et al. Enhancing the supercapacitor performance of graphene/ MnO_2 nanostructured electrodes by conductive wrapping. *Nano Lett.* **11**, 4438–4442 (2011).
- Han, G. et al. MnO_2 nanorods intercalating graphene oxide/polyaniline ternary composites for robust high-performance supercapacitors. *Sci. Rep.* **4**, 4824 (2014).
- Kaveevivitchai, W. & Jacobson, A. J. Exploration of vanadium benzenedicarboxylate as a cathode for rechargeable lithium batteries. *J. Power Sources* **278**, 265–273 (2015).
- Morozan, A. & Jaouen, F. Metal organic frameworks for electrochemical applications. *Energy Environ. Sci.* **5**, 9269–9290 (2012).
- Zhang, Z. Y., Yoshikawa, H. & Awaga, K. Monitoring the solid-state electrochemistry of Cu (2,7-AQDC) (AQDC=anthraquinone dicarboxylate) in a lithium battery: coexistence of metal and ligand redox activities in a metal–organic framework. *J. Am. Chem. Soc.* **136**, 16112–16115 (2014).
- Shin, J. et al. MIL-101 (Fe) as a lithium-ion battery electrode material: a relaxation and intercalation mechanism during lithium insertion. *J. Mater. Chem. A* **3**, 4738–4744 (2015).
- Hu, H., Guan, B., Xia, B. & Lou, X. W. Designed formation of $Co_3O_4/NiCo_2O_4$ double-shelled nanocages with enhanced pseudocapacitive and electrocatalytic properties. *J. Am. Chem. Soc.* **137**, 5590–5595 (2015).
- Hu, H., Han, L., Yu, M., Wang, Z. & Lou, X. W. Metal–organic-framework-engaged formation of Co nanoparticle-embedded carbon@ Co_3S_4 double-shelled nanocages for efficient oxygen reduction. *Energy Environ. Sci.* **9**, 107–111 (2016).

26. Tanabe, K. K. & Cohen, S. M. Postsynthetic modification of metal–organic frameworks—a progress report. *Chem. Soc. Rev.* **40**, 498–519 (2011).
27. Wang, Z. Q. & Cohen, S. M. Postsynthetic modification of metal–organic frameworks. *Chem. Soc. Rev.* **38**, 1315–1329 (2009).
28. Ferey, G. et al. Mixed-valence Li/Fe-based metal–organic frameworks with both reversible redox and sorption properties. *Angew. Chem., Int. Ed.* **46**, 3259–3263 (2007).
29. Fateeva, A. et al. Synthesis, structure, characterization, and redox properties of the porous MIL-68 (Fe) solid. *Eur. J. Inorg. Chem.* **2010**, 3789–3794 (2010).
30. Meilikhov, M. et al. Reduction of a metal–organic framework by an organo-metallic complex: magnetic properties and structure of the inclusion compound $[(\eta^5\text{-C}_5\text{H}_5)_2\text{Co}]_{0.5}@\text{MIL-47(V)}$. *Angew. Chem., Int. Ed.* **49**, 6212–6215 (2010).
31. Li, W., Liu, J. & Zhao, D. Mesoporous materials for energy conversion and storage devices. *Nat. Rev. Mater.* **1**, 1–17 (2016).
32. Davis, M. E. Ordered porous materials for emerging applications. *Nature* **417**, 813–821 (2002).
33. Slater, A. G. & Cooper, A. I. Function-led design of new porous materials. *Science* **348**, 6238 (2015).
34. Wu, Z. X. & Zhao, D. Y. Ordered mesoporous materials as adsorbents. *Chem. Commun.* **47**, 3332–3338 (2011).
35. Walcarius, A. Mesoporous materials and electrochemistry. *Chem. Soc. Rev.* **2**, 4098–4140 (2013).
36. Linares, N., Silvestre-Albero, A. M., Serrano, E., Silvestre-Albero, J. & Garcia-Martinez, J. Mesoporous materials for clean energy technologies. *Chem. Soc. Rev.* **43**, 7681–7717 (2014).
37. Wan, Y. & Zhao, D. Y. On the controllable soft-templating approach to mesoporous silicates. *Chem. Rev.* **107**, 2821–2860 (2007).
38. Guo, J. et al. Modular assembly of superstructures from polyphenol-functionalized building blocks. *Nat. Nanotechnol.* **11**, 1105–1111 (2016).
39. Umh, H. N. et al. Lithium metal anode on a copper dendritic superstructure. *Electrochem. Commun.* **99**, 27–31 (2019).
40. Gu, B. et al. Rationally assembled porous carbon superstructures for advanced supercapacitors. *Chem. Eng. J.* **361**, 1296–1303 (2019).
41. Yan, Y. et al. Bundled and dispersed carbon nanotube assemblies on graphite superstructures as free-standing lithium-ion battery anodes. *Carbon* **142**, 238–244 (2019).
42. Tong, Y. et al. Tube-in-tube tin dioxide superstructures with enhanced lithium storage performance. *Chem. Commun.* **55**, 2222–2225 (2019).
43. Ma, K., Jiang, H., Hu, Y. & Li, C. 2D nanospace confined synthesis of pseudocapacitance-dominated $\text{MoS}_2\text{-in-Ti}_3\text{C}_2$ superstructure for ultrafast and stable Li/Na-ion batteries. *Adv. Funct. Mater.* **28**, 1804306 (2018).
44. Zhang, Y. et al. MXene/Si@SiOx@C layer-by-layer superstructure with auto-adjustable function for superior stable lithium storage. *ACS Nano* **132**, 2167–2175 (2019).
45. Zuo, Y. et al. A high-capacity O_2 -type Li-rich cathode material with a single-layer Li_2MnO_3 superstructure. *Adv. Mater.* **30**, 1707255 (2018).
46. Vimalanathan, K. et al. Surfactant-free fabrication of fullerene C60 nanotubes under shear. *Angew. Chem. Int. Ed.* **56**, 8398–8401 (2017).
47. Liu, D., Zhao, W., Liu, S., Cen, Q. & Xue, Q. Comparative tribological and corrosion resistance properties of epoxy composite coatings reinforced with functionalized fullerene C60 and grapheme. *Surf. Coat. Tech.* **286**, 354–364 (2016).
48. Roy, X. et al. Nanoscale atoms in solid-state chemistry. *Science* **341**, 157–160 (2013).
49. Ardhi, R. E. A. et al. Self-relaxant superelastic matrix derived from C60 incorporated Sn nanoparticles for ultra-high-performance Li-ion batteries. *ACS Nano* **12**, 5588–5604 (2018).
50. Zhang, X. et al. $\text{LiFePO}_4/\text{NaFe}_3\text{V}_9\text{O}_{19}$ /porous glass nanocomposite cathodes for Li+/Na+ mixed-ion batteries. *J. Mater. Chem. A* **3**, 22247–22257 (2015).
51. Zhang, X. et al. Fabricating high-energy quantum dots in ultra-thin LiFePO_4 nanosheet using a multifunctional high-energy biomolecule—ATP. *Energy Environ. Sci.* **7**, 2285–2294 (2014).
52. Jin, Y. et al. Structural and optoelectronic properties of C60 rods obtained via a rapid synthesis route. *J. Mater. Chem.* **16**, 3715–3720 (2006).
53. Cui, C.-X. & Liu, Y.-J. Role of encapsulated metal cation in the reactivity and regioselectivity of the C60 Diels–Alder reaction. *J. Phys. Chem. A* **119**, 3098–3106 (2015).
54. Farid, G. & Kruk, M. Silica nanotubes with widely adjustable inner diameter and ordered silicas with ultralarge cylindrical mesopores templated by swollen micelles of mixed pluronic triblock copolymers. *Chem. Mater.* **29**, 4675–4681 (2017).
55. Fan, L. & Lu, B. Reactive oxygen-doped 3D interdigital carbonaceous materials for Li and Na ion batteries. *Small* **12**, 2783–2791 (2016).
56. Luo, W. et al. Electrochemically expandable soft carbon as anodes for Na-ion batteries. *ACS Cent. Sci.* **1**, 516–522 (2015).
57. Brougham, C. M. et al. Freeze-drying as a novel biofabrication method for achieving a controlled microarchitecture within large, complex natural biomaterial scaffolds. *Adv. Healthc. Mater.* **6**, 1700598 (2017).